Structure evolution mechanism of $Na_{0.5}Bi_{2.5}Nb_{2-x}W_xO_{9+\delta}$ ferroelectric ceramics: Temperature-dependent optical evidence and first-principles calculations

Qianqian Li (李欠欠),[1] Junyong Wang (王军勇),[1] Mengjiao Li (李梦姣),[1] Shuang Guo (郭爽),[1] Jinzhong Zhang (张金中),[1] Zhigao Hu (胡志高),[1,*] Zhiyong Zhou (周志勇),[2] Genshui Wang (王根水),[2] Xianlin Dong (董显林),[2] and Junhao Chu (褚君浩)[1]

[1]*Key Laboratory of Polar Materials and Devices (MOE) and Technical Center for Multifunctional Magneto-Optical Spectroscopy (Shanghai), Department of Electronic Engineering, East China Normal University, Shanghai 200241, China*

[2]*Key Laboratory of Inorganic Functional Materials and Devices, Shanghai Institute of Ceramics, Chinese Academy of Sciences, Shanghai 200050, China*

(Received 20 April 2017; revised manuscript received 15 June 2017; published 5 July 2017)

The effects of W doping on the structure and optical properties of Aurivillius ferroelectric $Na_{0.5}Bi_{2.5}Nb_2O_9$-based ceramics have been investigated by x-ray diffraction, far-infrared reflectance, and spectroscopic ellipsometry (SE). Moreover, the temperature dependent lattice dynamics and electronic properties have been systemically explored by Raman scattering (77–800 K) and SE (200–800 K), respectively. The anomalous temperature dependence of phonon frequencies around 600 K can be ascribed to the existence of an intermediate phase between ferroelectric orthorhombic and paraelectric tetragonal phases, which is also confirmed by temperature dependent electronic transitions extracted by the SE technique. In addition, the intrinsic evolution mechanism of the structure and electronic transitions during the phase transitions has been clarified by first-principles calculations, which indicate the effective application of noncontact optical methods in judging the phase transformations of ferroelectric materials.

DOI: 10.1103/PhysRevB.96.024101

I. INTRODUCTION

Bengt Aurivillius first described the structures of the mixed bismuth-oxide layer-structure compounds in 1949 and the possible ferroelectric nature of the Aurivillius phase was discovered a decade later [1–3]. Recently, the bismuth layer-structured ferroelectrics (BLSFs) with Aurivillius phase have gained increasing attention since $SrBi_2Nb_xTa_{2-x}O_9$ based random-access memory reported by Araujo [4]. The remarkable character of relatively high Curie temperature (T_c), low dielectric dissipation, strong anisotropic electromechanical properties, and high mechanical quality factors make BLSFs available for high temperature sensor applications [4,5]. The general chemical formula of BLSFs is $(Bi_2O_2)^{2+}(A_{m-1}B_mO_{3m+1})^{2-}$, where A is a mono-, di-, or trivalent element with a large 12 coordinate cation, B is a transition metal element with a 6 coordinate cation, and m is an integer (vary from 1 to 6) representing the number of octahedral layers [3,6,7]. The spontaneous polarization in the ferroelectric phase of BLSFs is suggested to originate from several displacive mechanisms involving the rigid displacement along the polar a axis, as well as rotations around the a axis and the c axis [7,8]. However, the piezoelectric activity and electrical resistivity of these materials are relatively low at elevated temperature because of two-dimensional orientation restriction of the rotation and the high coercive fields, which limit the potential high-temperature applications [9,10]. Fortunately, it has been reported that suitable doping can increase the electrical resistivity and improve the piezoelectric activity, achieving a compromise between good polarizability and high T_c [10–16]. Therefore, it is necessary to deeply investigate the structure evolution with the doping and temperature for future high temperature applications.

As a typical BLSF, $Na_{0.5}Bi_{2.5}Nb_2O_9$ (NBNO) has gained much attention since the relatively high T_c (770 °C) was reported in 1977 [17]. The structural and dielectric properties of modified NBNO ceramics have been studied previously. Our previous work indicated that B-site substitution of Nb^{5+} by W^{6+} not only enhances the piezoelectric activity ($d_{33} = 21.8$ pC/N), but also increases the electrical resistivity by about two orders of magnitude compared that of pure NBNO ceramic [12]. However, the doping effects on structure distortion and physical properties of W-modified NBNO ceramics have not been well investigated. The phase transformation is described as a tetragonal prototype ($I4/mmm$) at high temperature above Curie temperature and orthorhombic ($A2_1am$) at room temperature, only slightly distorted from tetragonal [18]. However, it is still an open issue whether there is an intermediate phase (e.g., space group $Amam$ of $SrBi_2Ta_2O_9$ [19]) during the phase transformation for NBNO ceramic. Recently, it was reported that NBNO may undergo a phase transformation from an orthorhombic phase to a pseudotetragonal phase above 200 °C then to a tetragonal phase. Nevertheless, the intermediate phase was not identified due to the similar structure between pseudotetragonal and tetragonal from x-ray diffraction (XRD) experiments [14]. As we know, Raman scattering and infrared reflectance (IR) spectra are nondestructive and attractive probe techniques, which are complementary and can provide some invaluable information on lattice vibrations and structural variations [20–22]. It is reported that temperature dependent phonon modes are effective strategies to explore the origin of lattice instabilities and phase transformations [19,23,24]. On the other hand, spectroscopic ellipsometry (SE) is an effective method for determining the dielectric functions of materials, which are required for applications as a dielectric material. In particular,

*zghu@ee.ecnu.edu.cn

the imaginary part of the dielectric functions is directly related to the band structures and electronic transitions. Note that temperature effects on the electronic transitions can give an important insight on the pyroelectric, ferroelectric, and dielectric properties of ferroelectric oxides [25–27]. Therefore, it is necessary to further investigate the physical mechanism with the aid of spectral experiments under different conditions (such as doping and temperature), which can induce the structural and electronic state variations.

In this work, the structure distortion with different W content has been studied by XRD, far-infrared reflectance (FIR) spectra, and SE. The optical phonon modes and electronic transitions extracted by temperature dependent Raman and SE spectra are applied to further clarify the intrinsical phase behaviors of NBNWx ceramics. Moreover, the physical mechanisms of electronic transitions are explained with the aid of the first-principles calculations. Finally, based on the analysis of the thermal evolutions and theoretic evidence, intermediate phase transformations can be determined.

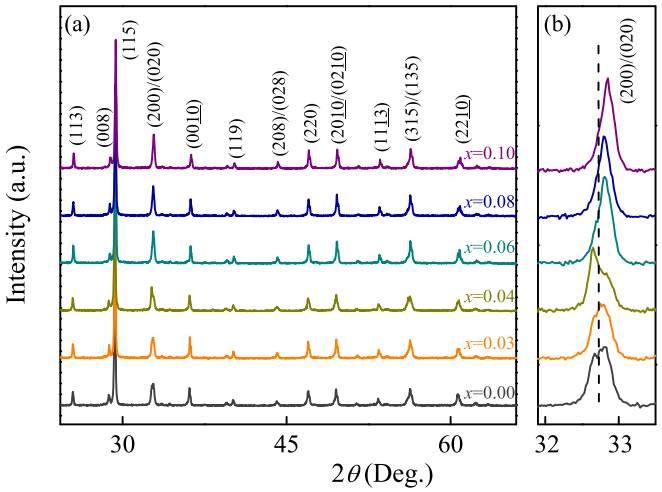

FIG. 1. (a) The XRD patterns and (b) enlaged XRD patterns of the NBNWx ceramics at room temperature. Note that each spectrum is shifted in intensity for clarity.

II. EXPERIMENTAL DETAILS

Aurivillius $Na_{0.5}Bi_{2.5}Nb_{2-x}W_xO_{9+\delta}$ (NBNWx, $x = 0.00$, 0.03, 0.04, 0.06, 0.08 and 0.10, abbreviated as NBNO, NBNW3, NBNW4, NBNW6, NBNW8 and NBNW10, respectively) ceramics were prepared by a solid state reaction method. The precursor materials were high purity Bi_2O_3 (99.90%), Nb_2O_5 (99.90%), Na_2CO_3 (99.80%), and WO_3 (99.90%). The samples were pressed into disks with a diameter of 15 mm and 1.5 mm in thickness and then sintered for 2 h at 1100 °C. The ceramics were ground to a final dimension of 12 mm in diameter and 0.5 mm in thickness and then single-side polished and cleaned in pure ethanol with an ultrasonic bath and rinsed several times by deionized water before spectral measurements. The detailed preparation process could also be found in Ref. [12].

The crystalline structures of NBNWx ceramics were investigated by XRD using a Ni filtered Cu $K\alpha$ radiation source (D/MAX-2550 V, Rigaku Co.). A vertical goniometer (Model RINT2000) was used in the XRD measurement, and continuous scanning mode (θ–2θ) with a scanning rate of 10°/min and interval of 0.02° was selected. FIR spectra of the NBNWx ceramics were measured by a Bruker Vertex 80V Fourier transform infrared spectrometer (Bruker Co., Billerica, MA) equipped with a specular reflectance setup. The externally incident angle was set as 6°. A gold mirror was adopted as a reference for the FIR spectra because of its absolute reflectance, and its amplitude was recorded. Temperature dependent Raman scattering measurements were carried out by a micro-Raman spectrometer with a spectral resolution of 1 cm^{-1} (Jobin-Yvon LabRAM HR 800 UV) in the temperature range of 77–800 K with a step of 25 K, and the precision was about 0.5 K. A He-Ne laser with the wavelength of 632.8 nm was taken as the exciting source. The laser beam was focused through a 50× microscope with a working distance of 18 mm. An air cooled charge coupled device (CCD) (−70 °C) with a 1024 × 256 pixels front illuminated chip was used to collect the scattered signal dispersed on 1800 grooves/mm grating. On the other hand, the ellipsometric measurements were carried out by near infrared-ultraviolet spectroscopic ellipsometry in the photon energy range of 2.3–5.7 eV (V-VASE by J. A. Woollam Co., Inc.). The spectral resolution was set to 5 nm and the incident angle was fixed to 70°. The temperature range could be varied from 200 to 800 K using an Instec cell with liquid nitrogen cooling accessory and frame water pump cooling (Janis ST-400). The step was 25 K and the set-point stability was better than 1 K. The ellipsometric data were fitted by the software package WVASE32, which allows window corrections to be included as a part of the model during the analysis process.

III. RESULTS AND DISCUSSION

A. Structural analysis

Figure 1 illustrates the XRD patterns of W-doped NBNO ceramics measured at room temperature. As shown in Fig. 1(a), the main phase of $Na_{0.5}Bi_{2.5}Nb_2O_9$ (JCPDF No. 00-049-0608) suggests that all NBNWx samples belong to the orthorhombic phase with the space group $A2_1am(36)$. It indicates that W^{6+} ions diffused Nb^{5+} ions on the B site of the NBNO matrix as desired since there are no secondary phases. The highest diffraction near 29.4° can be assigned to a (115) peak, which is consistent with the strongest diffraction peak ($112n + 1$) of the Aurivillius phase [15]. In order to further analyze the structure evolution of NBNWx ceramics, the enlarged XRD patterns in the range of 2θ from 31.9° to 33.5° are shown in Fig. 1(b). It is clear that the (200)/(020) diffraction peak can be identified by two distinguishable peaks when $x \leqslant 0.04$. However, the (200) peak and (020) peak tend to merge into a single peak when $x \geqslant 0.06$, which can be attributed to a smaller ionic radius and higher value state of W^{6+} [0.60 Å with a coordination number (CN) = 6] than that of Nb^{5+} (0.64 Å with CN = 6). Such phenomenon can also be found in W doped $CaBi_2Nb_2O_9$ ceramics [28]. Moreover, the merger of (200) and (020) diffraction peaks can indicate the increase of the lattice symmetry of materials [14]. Therefore, it can be concluded that the lattice symmetry of

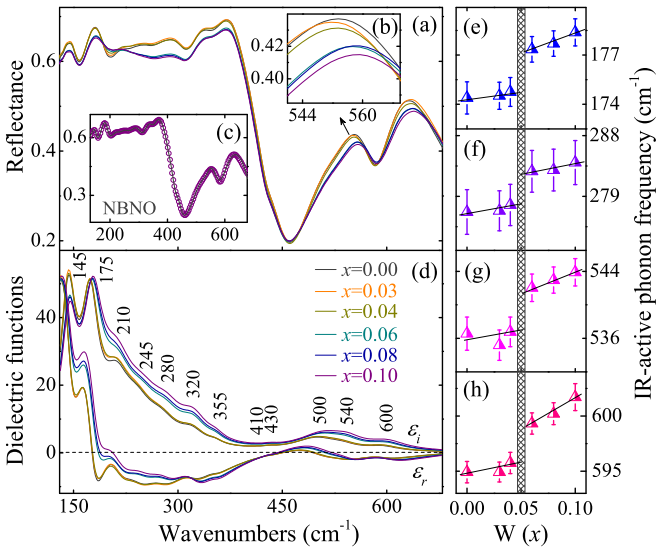

FIG. 2. (a) FIR spectra of the NBNWx ceramics at room temperature; (b) enlarged parts in the range of 540–570 cm^{-1}; (c) the experimental (dotted line) and the best fitting (solid line) FIR spectra of NBNO. (d) Real (ε_r) and imaginary (ε_i) parts of dielectric functions extracted by fitting FIR spectra with a multi-Lorentzian oscillator model. (e)–(h) The various frequency trends of some typical infrared-active phonons with increasing W content. The solid lines are a guide for the eyes to emphasize the various trends.

the ceramics with high W content ($x > 0.04$) is prominently improved as compared to those with low W content ($x \leqslant 0.04$).

To further explore the structure variation with the W content, the lattice vibrations of NBNWx ceramics were investigated. Vibrational studies can be used to detect the displacements of atoms or ions, some of which are related to the polarization of the material. Raman scattering and IR spectra are useful tools to explore the microscopic origin of the ferroelectricity and detect the local order changes, especially the significant variation in the anion-cation bond forces. The theoretical calculation of phonons in the $A2_1am$ space group of some two-layer Aurivillius materials, such as $ABi_2Nb_2O_9$ (A = Ca, Sr, Ba) were previously reported [21]. For the orthorhombic phase ($A2_1am$, C_{2v}^{12}), group theoretical analysis provides the optical modes as $\Gamma^{\text{opt.}} = 21A_1$ (R,IR) + $20A_2$ (R) + $19B_1$ (R,IR) + $21B_2$ (R, IR), where R and IR stand for Raman-active and infrared-active phonons, respectively [29].

Figure 2(a) shows the IR spectra of NBNWx ceramics in the range between 120 and 700 cm^{-1} at room temperature. It can be seen that the reflectivity of NBNW6, NBNW8, and NBNW10 is higher than that of NBNO, NBNW3, and NBNW4 at a certain frequency region. The detailed separation trend of infrared bands in the range of 540–570 cm^{-1} is shown in Fig. 2(b). To further analyze the effect of W content, a fitting procedure using the multi-Lorentzian oscillator functions was carried out. It is difficult to resolve all modes in the spectrum on account of possible modes overlapping and/or their small intensities. Therefore, we discerned 12 modes to fit the experimental spectra, and the well-fitted infrared reflectance spectrum of NBNO is shown in Fig. 2(c). Moreover, the dielectric functions can be derived through Fresnel's formula [30]: $R(\omega) = |\tilde{\varepsilon}(\omega)^{1/2} - 1|^2/|\tilde{\varepsilon}(\omega)^{1/2} + 1|^2$. The real $\varepsilon_r(\omega)$ and imaginary $\varepsilon_i(\omega)$ parts of dielectric functions of NBNWx are plotted in Fig. 2(d) and the positions of the 12 modes are assigned. The frequency trends of some typical infrared-active phonons with increasing W content are shown in Figs. 2(e)–2(h).

Because of the large atom number of the crystal unit cell and complicated crystal structure, the mode assignments for NBNO materials are still not clear. By reference to the theoretical calculation of $ABi_2Nb_2O_9$ (A = Ca, Sr, Ba) and $SrBi_2Ta_2O_9$ [21,22], some typical modes assignments for NBNWx are described as follows. The mode near 175 cm^{-1} is ascribed to the interactions of A- and B-site atoms with the equatorial oxygen atom of the octahedron. The mode at about 280 cm^{-1} is related to the Bi-O (the apex oxygen atom of the octahedral) stretching bonds while the Bi-O bonds in the bismuth layers contribute to the frequency around 540 cm^{-1}. The mode around 600 cm^{-1} belongs to the octahedral bending modes, which are mainly caused by the motion of the equatorial oxygen atom of the octahedron. The four typical modes revealed in Figs. 2(e)–2(h) show a blueshift with increasing W content. It indicates that the B-site cation vibration and the cationic vibration in $(Bi_2O_2)^{2+}$ layers are influenced by W^{6+} substitutions. As we know, the W^{6+} substitution would likely introduce some cationic vacancies to maintain the electroneutrality, which may affect the structure variation in the $(Bi_2O_2)^{2+}$ layer. Besides, the obvious increment between NBNW4 and NBNW6 ceramics indicates the remarkable distortion of structure variation, which is consistent with the XRD results. The structural distortion induced by W^{6+} can be obtained by considering the tolerance factor $t = (R_A + R_O)/\sqrt{2}(R_B + R_O)$, where R_A, R_B, and R_O are the ionic radii of A (Bi^{3+} and Na^{+}) and B (Nb^{5+} and W^{6+}) cations and O^{2-} anions, respectively. The average ionic radius appropriately matches the A-O or B-O length in a cubic cell ($t = 1$). When $t < 1$, the B-O bond is longer than the A-O one. Therefore, the A-O-A structure exerts a contraction on the corner-connected octahedra, which will rotate to keep the B-O bond length [31]. In the case of substitution of Nb^{5+} by W^{6+}, the t increases with increasing W content since the W^{6+} ionic radius (0.60 Å) is slightly smaller than that of Nb^{5+} (0.64 Å). The tensile stress on W-O bonds in NBNWx ceramics will induce higher dielectric constants [32].

B. Raman scattering

Temperature dependent Raman spectra were recorded to elucidate the thermal evolution of NBNWx ceramics. As an example, Figs. 3(a) and 3(b) show Raman spectra of NBNO and NBNW6 ceramics at different temperatures. At low temperature, the weak Raman peaks/shoulders cannot be assigned since they come from the first- or second-order Raman scattering and complicated asymmetric structure. Some modes in the range of 250–400 cm^{-1} gradually become weaker with increasing the temperature and finally disappear, indicating the reduction of structural distortion and the improvement of symmetry. The modes near 590 cm^{-1} exhibit a slight redshift with increasing temperature, which can be ascribed to the thermal expansion of lattice and anharmonic phonon-phonon interactions. As a function of temperature it can be expressed by the perturbation model, which is written

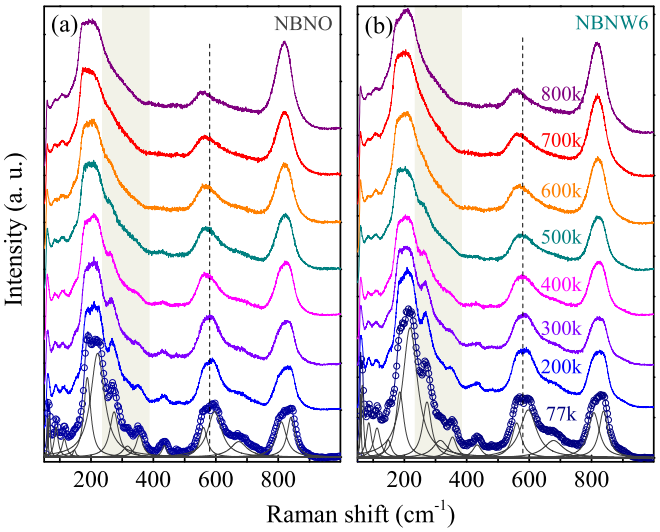

FIG. 3. Raman spectra of (a) NBNO and (b) NBNW6 ceramics at different temperature after correcting for thermal population factor and the corresponding multi-Lorentz peak fitting at 77 K. For clarity, each spectrum is shifted in intensity.

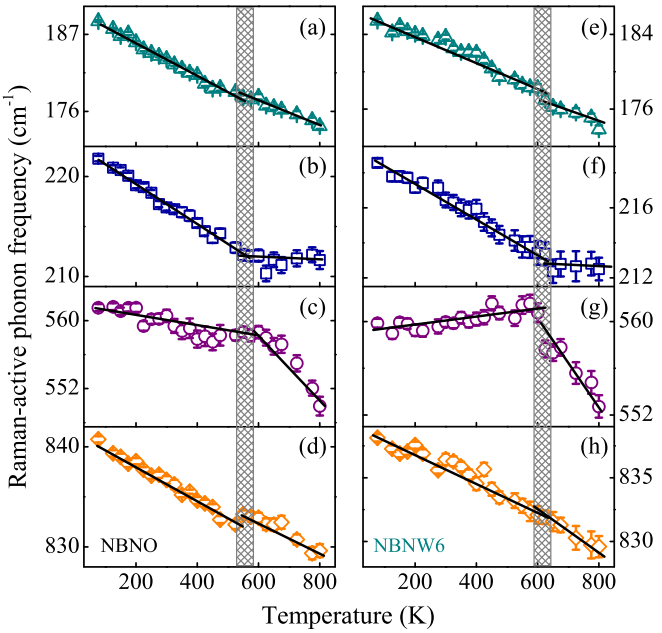

FIG. 4. The various frequency trends of some typical Raman-active modes with increasing temperature for (a)–(d) NBNO and (e)–(h) NBNW6 ceramics. The shaded stripes show the boundaries of adjacent phases and the solid lines are a guide for the eyes to emphasize the various trends.

as [33] $\omega(T) = \omega_0 + \Delta\omega_e(T) + \Delta\omega_d(T)$, where $\Delta\omega_e(T) = -\omega_0\gamma \int_0^T [\alpha_a(T) + \alpha_b(T) + \alpha_c(T)]dT$, $\Delta\omega_d(T) = A[1 + 2/(n_1 - 1)] + B[1 + 3/(n - 1) + 3/(n - 1)^2]$ + higher order terms, $n_1 = \exp(\hbar\omega_0/2k_BT)$, and $n = \exp(\hbar\omega_0/3k_BT)$. The γ is Grüneisen parameter. The parameters α_a, α_b, and α_c are the thermal expansion coefficients in the a, b, and c axes, respectively. It should be emphasized that the first term ω_0 represents the harmonic frequency of the optical mode and the second one is related to the thermal expansion of the lattice. Moreover, the third one corresponds to cubic, quadratic, and higher order anharmonic coupling between phonons. Therefore, the redshift of mode frequency with increasing temperature is mainly due to the thermal expansion. In addition, the low-frequency shifting, the weakening, and the disappearing of Raman modes against temperature can suggest a symmetry change [16].

In order to determine the temperature evolution of Raman modes, all experimental spectra were decomposed into a series of bands with the multi-Lorentzian oscillator approximation. Notably, all spectra were corrected for the Bose-Einstein temperature factor in the fitting process to eliminate the contribution of the Bose-Einstein population factor from the measured scattering intensity [34]. By fitting the Raman spectra, some typical temperature dependent phonon frequencies are extracted and shown in Fig. 4. Theoretically, Raman modes at 180 and 215 cm^{-1} are associated with the $a(b)$- and c-axis vibrations of the B-site ions, respectively [24]. The modes around 560 cm^{-1} mainly result from the the vibration of Bi-O bonds in the $(Bi_2O_2)^{2+}$ layers, and the mode near 830 cm^{-1} is dominated by the vibration of equatorial oxygen atoms in the Nb-O plane [21,22]. From Fig. 4, it is apparent that the typical modes show an obvious redshift with the temperature, which can be ascribed to the thermal expansion of the lattice and anharmonic phonon-phonon interactions as mentioned above. However, the abnormal phonon shift beyond about 500 K for NBNO and 610 K for NBNW6 cannot be only explained by the temperature effect, which may illustrate that there is one intermediate phase transformation ($T^* \sim 500$ K for NBNO, and $T^* \sim 610$ K for NBNW6) in the temperature range of 77–800 K. As observed in $SrBi_2Ta_2O_9$ and Bi_3TiNbO_9, the subtle change of Raman modes upon heating suggested an intermediate symmetry between the ferroelectric $A2_1am$ phase and the paraelectric $I4/mmm$ phase [24,35]. Hence, it is reasonable to consider the anomaly as an intermediate phase transformation before the ferroelectric transformation appears. Especially, the mode near 830 cm^{-1} is dominated by the apparent vibration of equatorial oxygen ions in the Nb-O plane, which is not sensitive to the temperature. Moreover, the structural change of the intermediate phase transformation is relatively weak, as compared to the following ferroelectric phase transformation at about 1043 K, which is usually ignored by simply structural analysis. Thus, more research is necessary to confirm the intermediate phase transformations of NBNWx ceramics.

C. Spectroscopic ellipsometry

Spectroscopic ellipsometry is a sensitive and nondestructive optical technique, which can measure the relative changes in the amplitude and phase in the particular direction of polarized lights upon oblique reflection from the sample surface. The experimental parameters measured by ellipsometry are the complex ratio $\tilde{\rho}(h\nu)$ in terms of $\Psi(h\nu)$ and $\Delta(h\nu)$, which are a function of the incident angle, photon energy $h\nu$, and optical functions $\tilde{\varepsilon}(h\nu)$ of measured materials [36]. In order to extract the dielectric functions $[\tilde{\varepsilon}(h\nu) = \varepsilon_r(h\nu) + i\varepsilon_i(h\nu)]$ and other physical parameters of NBNWx ceramics, we modeled a three-layer structure (air/surface rough layer/ceramic) to

evaluate the ellipsometric spectra [37]. The surface rough layer is taken into account by the Brüggeman effective medium approximation (EMA), which is described by the assumption of 50% void component and 50% NBNWx bulk material [38]. Tauc-Lorentz and Gaussian oscillator models were used, which can abide by Kramers-Kroning constraints [39]. A single Tauc-Lorentz oscillator defined the optical band gap E_g, and the best fit resulted from the addition of one Gaussian oscillator. The Gaussian oscillator was placed above the E_g in the fitting process, which represents a band-to-band transition [40]. Moreover, it is well known that the band structure observed in the dielectric spectra is attributed to interband transitions. Consequently, a standard critical point (SCP) model was performed to study the temperature evolution of interband transitions. The SCP model is defined as [25] $\tilde{\varepsilon}(h\nu) = C - Ae^{i\theta}(h\nu - h\nu_k + i\Gamma)^n$. Here, A is the amplitude to describe the critical point, θ is the excitonic phase angle, $h\nu_k$ is the electronic transition, and Γ is the broadening. In addition, the values of the exponent n are -0.5, 0 [$\ln(h\nu - h\nu_k + i\Gamma)$], and 0.5 for one-, two-, and three-dimensional critical points, respectively. Correspondingly, we calculated numerically the second partial derivative of the dielectric function $\partial^2\tilde{\varepsilon}/\partial(h\nu)^2$ to determine the electronic transitions in dielectric spectra and perform a line-shape analysis of the critical point. The expression of the second derivative can be written as follows:

$$\frac{\partial^2\tilde{\varepsilon}}{\partial(h\nu)^2} = Be^{i\theta}(h\nu - h\nu_k + i\Gamma)^{n-2}. \quad (1)$$

Specifically, the $\partial^2\tilde{\varepsilon}/\partial(h\nu)^2$ values were directly calculated by the original data because the surface roughness layer mainly affects the electronic transition intensity at other than the center energy.

Figure 5(a) and 5(b) show the the experimental ellipsometric and the best fitting spectra Ψ and Δ of NBNW4 and NBNW6 ceramics at room temperature. A good agreement between the experimental and calculated spectra can be found in the entire measured photon energy range. The thickness of roughness layer was obtained (3 ± 1 nm) for NBNWx ceramics, which is in common with the results of atomic force microscopy (AFM). The derived dielectric functions of the NBNWx ceramics in the photon energy range of 2.3–5.7 eV are shown in Fig. 5(c). The dielectric constants ε_r and ε_i with the photon energy are the typical optical response behaviors of dielectric materials. It is remarkable that the imaginary parts ε_i of all NBNWx ceramics are close to zero below the absorption edges, indicating that there are no additional electronic transitions in the low energy region. With further increasing photon energy, ε_i shows a sudden increase, derived from a strong absorption (near about 3.5 eV), which shows the interband electronic transition from the valence band (VB) to the lowest conductive band (CB). Meanwhile, the parameter ε_r increases with the photon energy and approaches the maximum value around 4.3 eV, then decreases because of the known Van Hove singularities. The inset of Fig. 5(c) shows that the absorption edges of ε_i spectra have a blueshift with increasing W content. Figure 5(d) shows the model parameter E_g as a function of W content. It can be found that the value of E_g is about 3.5 eV for NBNWx ceramics, which is similar to some other Aurivillius layered materials such as $BaBi_2Nb_2O_9$ and $CaBi_2Nb_2O_9$ [41]. With the W content, the parameter E_g linearly increases from 3.46 to 3.56 eV, then remains at 3.56 eV. The increasing E_g with the W content is also observed in W doped $CaBi_2Nb_2O_9$ and it highlights that the band structure is changed by the substitutive atom [28].

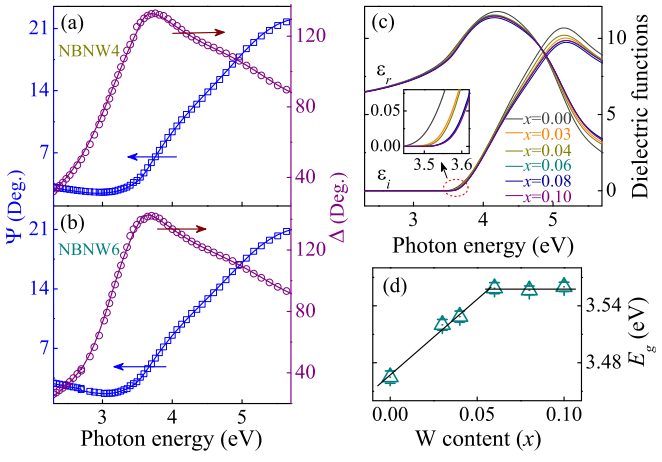

FIG. 5. The experimental ellipsometric (dots) and the best fitting (solid lines) spectra Ψ and Δ of (a) NBNW4 and (b) NBNW6 at room temperature. (c) The derived dielectric functions of the NBNWx ceramics. (d) The optical band gap (E_g) as a function of the W content.

To confirm the intermediate phase transformations of NBNWx ceramics, temperature dependent SE spectra have been recorded. Figs. 6(a)–6(c) display the derived real ε_r and imaginary ε_i parts of the dielectric functions for NBNO, NBNW4, and NBNW8 in the photon energy range of 2.3–5.7 eV at several temperatures, respectively. The imaginary parts ε_i of all NBNWx ceramics are in close proximity to zero in the region $E < E_g$. In the region $E > E_g$, the ε_i spectra are dominated by two intense interband excitonic absorption critical point (CP) features around 3.8 and 5.0 eV, marked by arrows in Figs. 6(a)–6(c) (hereinafter, E_{cp1} and E_{cp2}). The two CPs are inconspicuous in Figs. 6(a)–6(c); however, they can be clearly observed after calculating the second partial derivative spectra of the pseudodielectric function. Figure 6(d) shows the second partial derivative spectra for the imaginary part of NBNO at some temperatures as an example. Two evident dips dominate the derivative spectra, which indicates that there are two probed electronic transitions. Moreover, the second partial derivative spectra have a redshift trend with increasing temperature, which can be mainly ascribed to the temperature effects derived from the lattice thermal expansion and the band structure renormalization [25]. The accurate energies of CP features are obtained by fitting the second derivatives of the complex dielectric functions. Figure 6(e) shows the second derivatives of the complex dielectric functions spectra and the best-fitted spectra by the SCP model at 200, 400, and 700 K for NBNO, respectively. Table I displays the fitting parameters at some temperatures for comparison. The thermal evolution of interband electronic transition energies for NBNWx ceramics are plotted in Figs. 6(f)–6(i). The parameters E_{cp1} and E_{cp2} show a typical redshift trend with the temperature. The value of E_{cp1} gradually shifts to lower energy from 3.83 to 3.60 eV and the E_{cp2} shifts from 4.93 to 4.65 eV from 200 to 600 K for NBNO. Then, both of them remain nearly unchanged beyond

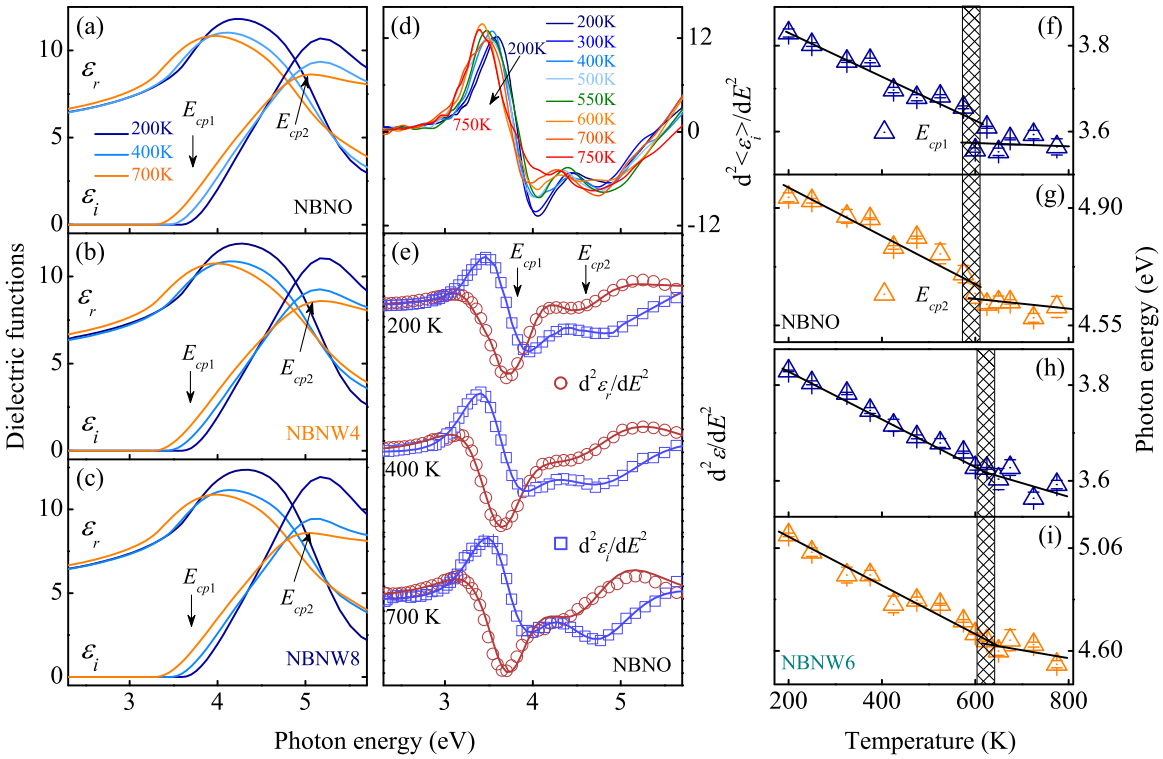

FIG. 6. The real and imaginary parts of the dielectric functions for NBNWx ceramics measured at 200, 400, and 700 K for NBNO (a), NBNW4 (b), and NBNW8 (c), respectively. (d) The second partial derivative spectra for the imaginary part of the pseudodielectric functions for NBNO at various temperatures. (e) The second derivatives of the dielectric functions spectra (symbols) and the best-fitted spectra (solid lines) at 200, 400, and 700 K for NBNO. Two interband transition E_{cp1} and E_{cp2} features are marked by arrows. (f)–(i) The thermal evolution of E_{cp1} and E_{cp2} energy for NBNO and NBNW6, respectively. The shaded stripes show the boundaries of adjacent phases and the solid lines a the guide for the eyes to emphasize the various trends.

600 K. For NBNW6, both E_{cp1} and E_{cp2} show different trends beyond about 610 K. The E_{cp1} is mainly dominated by A-cation p orbits and O-anion p orbits while E_{cp2} is associated tightly with B-cation d orbits [27]. On account of the complete symmetrical structure of paraelectric phase, the off-center B-site cation will travel smoothly to the center position of BO_6 along with the phase transformation from ferroelectric to paraelectric structure. The motion of the B-site

TABLE I. Parameters of the SCP model for NBNWx ceramics extracted from the best fitting second derivatives of the complex dielectric functions at several temperatures. Note that the 90% reliability of the fitting parameters is given in parentheses.

Samples	$x = 0.00$			$x = 0.03$			$x = 0.04$			$x = 0.06$			$x = 0.08$			$x = 0.10$		
T (K)	200	425	725	200	425	725	200	425	725	200	425	725	200	425	725	200	425	725
A_1	1.14	1.13	1.21	1.36	1.32	1.32	1.13	0.91	0.76	1.89	1.01	1.21	1.05	1.40	0.89	1.33	1.20	0.90
	(0.03)	(0.05)	(0.04)	(0.01)	(0.03)	(0.03)	(0.03)	(0.01)	(0.08)	(0.01)	(0.01)	(0.05)	(0.00)	(0.12)	(0.04)	(0.01)	(0.10)	(0.05)
ϕ_1 (deg)	14.2	13.7	13.5	14.5	14.2	13.9	14.0	13.8	12.9	14.7	14.4	13.4	14.4	13.8	13.4	14.4	14.0	13.6
	(0.04)	(0.05)	(0.06)	(0.01)	(0.01)	(0.03)	(0.02)	(0.03)	(0.19)	(0.01)	(0.06)	(0.05)	(0.01)	(0.03)	(0.03)	(0.02)	(0.06)	(0.01)
E_{cp1} (eV)	3.83	3.70	3.59	3.85	3.75	3.64	3.78	3.68	3.43	3.83	3.72	3.55	3.83	3.69	3.54	3.81	3.69	3.55
	(0.01)	(0.01)	(0.01)	(0.00)	(0.01)	(0.01)	(0.00)	(0.01)	(0.03)	(0.00)	(0.02)	(0.01)	(0.00)	(0.00)	(0.01)	(0.00)	(0.00)	(0.01)
Γ_1 (eV)	0.53	0.54	0.60	0.57	0.56	0.62	0.57	0.52	0.51	0.58	0.54	0.64	0.54	0.60	0.55	0.61	0.58	0.56
	(0.00)	(0.01)	(0.01)	(0.00)	(0.01)	(0.01)	(0.00)	(0.00)	(0.01)	(0.00)	(0.01)	(0.01)	(0.00)	(0.02)	(0.01)	(0.03)	(0.01)	(0.01)
A_2	5.11	6.92	9.02	3.45	4.21	5.31	11.85	7.05	10.2	3.88	5.10	8.30	5.89	5.41	9.76	6.27	6.16	7.78
	(0.19)	(0.42)	(0.15)	(0.21)	(0.03)	(0.25)	(0.30)	(0.19)	(0.07)	(0.05)	(0.09)	(0.10)	(0.04)	(0.18)	(0.07)	(0.10)	(0.42)	(0.16)
ϕ_2 (deg)	22.3	22.0	21.5	23.8	22.4	21.7	22.1	21.6	21.6	23.1	22.3	21.7	22.5	22.1	21.4	23.1	22.4	21.6
	(0.03)	(0.08)	(0.04)	(0.02)	(0.04)	(0.14)	(0.05)	(0.09)	(0.03)	(0.02)	(0.05)	(0.04)	(0.03)	(0.05)	(0.01)	(0.09)	(0.04)	(0.08)
E_{cp2} (eV)	4.93	4.78	4.57	5.34	4.90	4.59	4.83	4.60	4.47	5.12	4.81	4.63	4.95	4.83	4.52	5.14	4.87	4.53
	(0.01)	(0.01)	(0.01)	(0.00)	(0.01)	(0.05)	(0.05)	(0.01)	(0.01)	(0.01)	(0.02)	(0.02)	(0.02)	(0.01)	(0.00)	(0.03)	(0.02)	(0.02)
Γ_2 (eV)	1.13	1.26	1.38	0.92	1.03	1.18	1.65	1.33	1.45	1.11	1.23	1.34	1.22	1.15	1.39	1.35	1.31	1.30
	(0.01)	(0.03)	(0.07)	(0.02)	(0.01)	(0.02)	(0.02)	(0.01)	(0.01)	(0.01)	(0.01)	(0.01)	(0.01)	(0.02)	(0.01)	(0.02)	(0.04)	(0.02)

TABLE II. Optimized lattice parameters of NBNO for $A2_1am$, $Amam$, and $I4/mmm$.

	a (Å)	b (Å)	c (Å)	V (Å^3)
$A2_1am$	5.519	5.468	28.007	845.33
$Amam$	5.481	5.465	27.857	834.58
$I4/mmm$	3.915	3.915	25.008	383.37

cation affects the orbital hybridization between atoms in BO_6 octahedra, which leads to the evolution of E_{cp1} and E_{cp2} with the temperature. Therefore, the abnormal change of interband electronic transition energies E_{cp1} and E_{cp2} with temperature suggests structural transformation, which could be ascribed to the structural distortion induced by the intermediate phase transformation [27,42]. As we expect, the interband electronic transitions with temperature agree well with the results from Raman scattering. The observable intermediate phase transformation of NBNWx ceramics can be deduced to occur at about 600 K.

D. Physical mechanism

To further clarify the evolution of electronic band structure for NBNWx ceramics, first-principles calculation was performed. As far as we know, there has been no report about the structure of an intermediate phase for NBNO. Therefore, we chose space group $Amam$ as the reference structure by referring to similar systems ($SrBi_2Nb_2O_9$) [43]. The theoretical calculations were carried out only for NBNO to simplify the calculations. The generalized gradient approximation (GGA) of Perdew, Burke, and Ernzerhof (PBE) [44] for the exchange correlation interaction and the election interaction was employed along with a kinetic energy cutoff of 370 eV. The structure transitions of NBNO can be described by the ferroelectric orthorhombic in space group $A2_1am$ at room temperature, the paraelectric orthorhombic phase in reference space group $Amam$ near 600 K, and the paraelectric tetragonal structure in space group $I4/mmm$ above 1000 K. Structural optimizations were performed for the three phases and the ions were fully relaxed toward equilibrium until the residual forces on each atom were less than 0.03 eV/A. The corresponding structures and equilibrium lattice parameters are presented in Fig. 7 and Table II, respectively. Previous studies pointed out that the structural phase transformations are embodied in the degree of combined distortion, which involves the tilts of BO_6 octahedra and the displacement of B-site atoms in the octahedra [45]. In particular, the $A2_1am$ structure can be distinguished from the tetragonal structure by both the rotations of the NbO_6 octahedra and the displacement of atoms along the a axis from Fig. 7. In the paraelectric $Amam$ phase, the distortion of NbO_6 octahedra is decreasing. Moreover, the movement of the O atoms weakens the tilt about the c axis. There are no tilt and rotations of the NbO_6 octahedra in $I4/mmm$ tetragonal structure, ensuring the structural symmetry of the body-centered tetragonal system. In addition, the lattice constants in the present work are in reasonable agreement with the experimental values [11,43].

It has been verified that the orbital hybridization and covalency play a crucial role in structural distortion and band

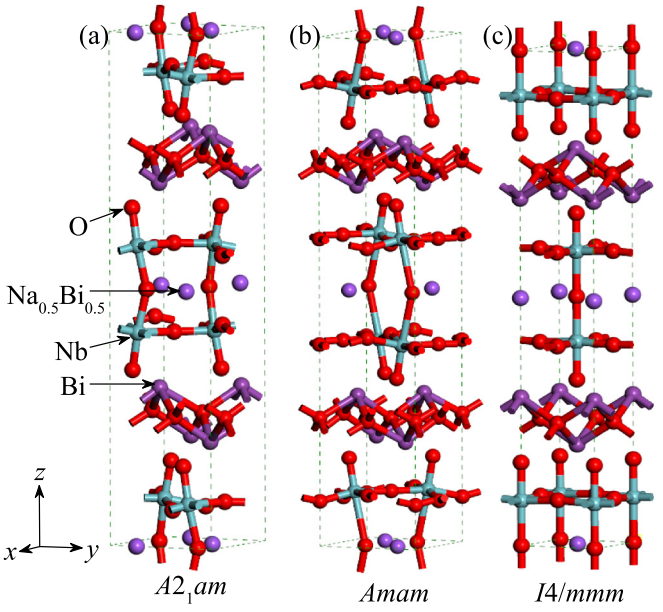

FIG. 7. Crystal structure of NBNO in three different phases. (a) Ferroelectric phase with space group $A2_1am$, (b) intermediate phase with possible space group $Amam$, (c) paraelectric phase with space group $I4/mmm$.

structure of ferroelectrics [46]. Figures 8(a)–8(c) show the band structure and density of states (DOS) of pure NBNO with different phases. The band structure of the paraelectric phase is quite different from those of ferroelectric and intermediate phases on account of the high symmetry structure. Detailed analysis shows that the leading interband transitions of the absorption edges derive from O-2p/Na-2p to Nb-4d for the three phases. The Na-2p state makes more contributions to the VB of paraelectric phase than that of the other phases, especially at the top of the VB. Moreover, the band gap of the paraelectric phase is indirect, while ferroelectric and intermediate phases have direct band gaps. Apparently, the top of the VB is predominantly constituted by the O-2p and Na-2p states and the bottom of the CB is dominated by Nb-4d, O-2p, and Bi-6p states. The direct electronic transition of the optical band gap is about 1.99 eV for the ferroelectric phase in Fig. 8(a), which fits well with similar Aurivillius layered materials such as $SrBi_2Ta_2O_9$ and $SrBi_2Nb_2O_9$ (2.44 and 2.35 eV, respectively) [43]. The optical band gap is about 1.61 eV for the intermediate phase and 1.66 eV for the paraelectric phase in Figs. 8(b) and 8(c), respectively. As a well-known problem of calculations based on density-functional theory (DFT), the calculated optical band gaps are underestimated by about 20%–30%, as compared to the experimental values. However, the variation trends between different phases are in good agreement with the experimental results in Figs. 6(f)–6(h). The narrower band gap of the paraelectric phase than that of ferroelectric phase can be attributed to the off-center displacements of the B-site cation and the buckling effect between the NbO_6 octahedra and the $(Bi_2O_2)^{2+}$ layer [43]. The distortion of structure can enhance the hybridization between Nb-4d and O-2p (the planar oxygen of octahedra) states and the hybridization between Bi-6s6p and O-2p (the apex oxygen of octahedra) states, which leads to a larger

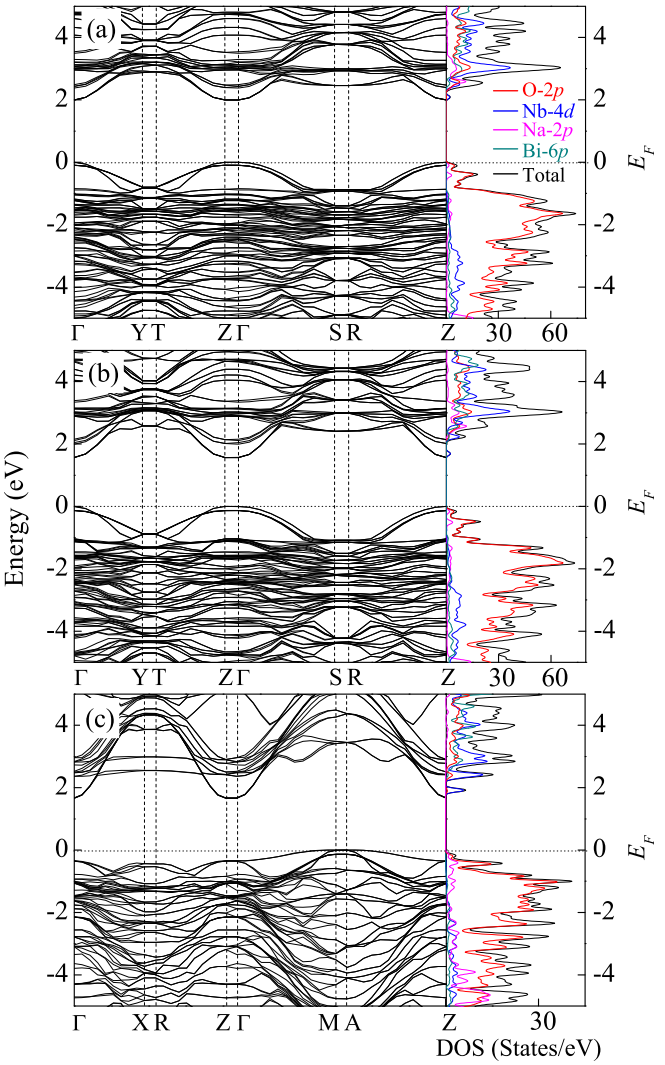

FIG. 8. Calculated band structure and corresponding density of states for (a) ferroelectric, (b) intermediate, and (c) paraelectric phases of NBNO.

band gap in the ferroelectric phase. Moreover, the change of optical band gap with the W content also can be explained by the first-principles calculation. As the W-5*d* orbital is more extended than the Nb-4*d* orbital, the W-5*d* state introduced in CBs will shift the bottom of conduction bands to higher energy states. Therefore, a suitable replacement could result in the enlargement of the band gap in NBNW*x*. The fact that the E_g remains at 3.56 eV with the W content more than 0.06 can be attributed to the changed of lattice symmetry. In principle, most of the interband transitions from ellipsometric spectra can be well supported by the density functional theory calculations [26,27,42]. This indicates that the variations of electronic transitions can be applied to judge the phase transformations in ferroelectric materials.

E. Phase diagram

Combining with experiments and theoretical analysis, a phase diagram with the intermediate phase of NBNW*x* has been completed. Figure 9 includes the present results and

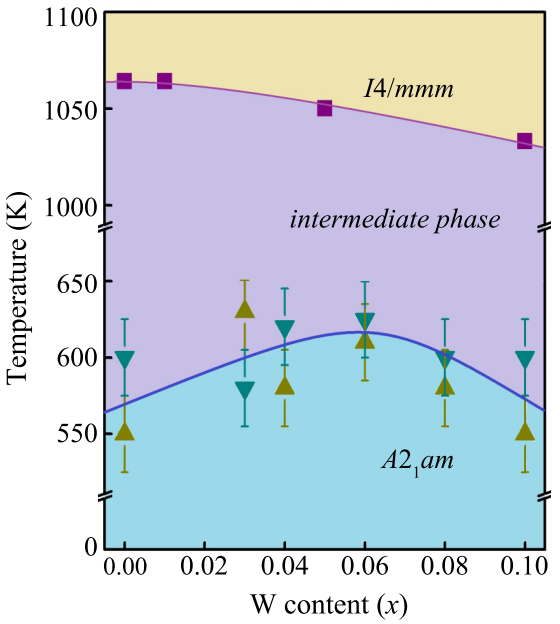

FIG. 9. Phase diagram of NBNW*x* ceramics with different W contents. The phase transformation temperatures in the present work are marked with the symbols ▲ for Raman and ▼ for SE results and the values marked by the symbol ■ are our previous work (Ref. [12]).

earlier studies of NBNW*x* ceramics [12]. The existence of the intermediate phase transformation is consistent with the basic paradigm from the Landau theory of structural phase transformations. It is established experimentally that these transformations involve approximate rotations of BO_6 octahedra and the displacement of ions along the *a* axis [47]. In the modern theory of polarization, a switching path connects the negatively oriented structure with opposite polarization, the positively oriented structure with its enantiomorphic counterpart. Hence, passing through an intermediate phase is crucially important. Although the actual switching path should obviously be more complex, the atomic positions are assumed to travel smoothly from positive to negative orientation through the intermediate phase. It is difficult to explain a phase transformation from ferroelectric orthorhombic phase to paraelectric tetragonal phase directly without an intermediate phase. Therefore, it is reasonable to consider the anomalies of phonon and CP shift with temperature as an intermediate of ferroelectric-paraelectric phase transformation before the ferroelectric transformation at about 1043 K. Nevertheless, it is clear that the intermediate phase transformations extracted from temperature dependent SE and Raman spectra are not at the same point in Fig. 9. This can be attributed to the unstable intermediate phase structure and the experimental temperature step of 25 K, which can induce the above errors. Combining with the results of temperature dependent Raman and SE spectra, the intermediate phase transformations between $I4/mmm$ and $A2_1am$ in W doped ceramics have been extracted to about 560 K for NBNO, 600 K for NBNW3, 600 K for NBNW4, 620 K for NBNW6, 600 K for NBNW8, and 560 K for NBNW10, as shown in Fig. 9. As mentioned above, the phase transformations of the ferroelectric materials would be reasonably related to the polarization. Therefore, the

determination of intermediate phase is important for future applications in high temperature devices.

IV. CONCLUSIONS

In conclusion, structure evolution of $Na_{0.5}Bi_{2.5}Nb_{2-x}W_xO_{9+\delta}$ ($x = 0$, 0.03, 0.04, 0.06, 0.08, and 0.10) ceramics with doping and temperature have been investigated by spectral experiments such as x-ray diffraction, far-infrared reflectance, Raman scattering, and spectroscopic ellipsometry. With increasing W content, the lattice symmetry has been improved and the optical band gap increases slightly from 3.46 to 3.56 eV, which can be attributed to the smaller ionic radius and higher valance state of W^{6+} (0.60 Å) than that of Nb^{5+} (0.64 Å). The intermediate phase transformation of $Na_{0.5}Bi_{2.5}Nb_2O_9$-based ceramics was first found by temperature dependent Raman scattering at about 600 K. Moreover, the appearance of phase transformations has been confirmed by the various trends of electronic transitions extracted by SE. With the aid of first-principles calculations for NBNO in different phases, the crystal structures have been determined. In addition, the redshift behavior of the absorption critical points E_{cp1} and E_{cp2} could be attributed to the B-site cation position and the buckling effect between the NbO_6 octahedra and $(Bi_2O_2)^{2+}$ layer. Finally, the phase diagram for NBNWx has been improved. The experimental and theoretical results clearly manifest that the phase transformation in ferroelectric materials could be discovered by noncontact and nondestructive optical methods.

ACKNOWLEDGMENTS

One of the authors (Q.Q.L.) is grateful to Dr. K. Jiang, Dr. L. Xu, and Dr. A. Cui for technical support. This work was financially supported by the Major State Basic Research Development Program of China (Grant No. 2013CB922300), the Natural and Science Foundation of China (Grants No. 61674057, No. 11374097, No. 61376129, No. 61504156, and No. 61227902), the Projects of Science and Technology Commission of Shanghai Municipality (Grants No. 15JC1401600 and No. 14XD1401500), and the Program for Professor of Special Appointment (Eastern Scholar) at Shanghai Institutions of Higher Learning.

[1] B. Aurivillius, Arkiv Kemi **1**, 499 (1949).
[2] G. A. Smolenskii, V. A. Isupov, and A. I. Agranovskaya, Sov. Phys. Solid State **1**, 400 (1959).
[3] E. C. Subbarao, J. Phys. Chem. Solids **23**, 665 (1962).
[4] C. A-Paz de Araujo, J. D. Cuchiaro, L. D. McMillan, M. C. Scott, and J. F. Scott, Nature (London) **374**, 627 (1995).
[5] S. J. Zhang and F. P. Yu, J. Am. Ceram. Soc. **94**, 3153 (2011).
[6] B. Frit and J. P. Mercurio, J. Alloys Compd. **188**, 27 (1992).
[7] H. Irie, M. Miyayama, and T. Kudo, J. Appl. Phys. **90**, 4089 (2001).
[8] R. L. Withers, J. G. Thompson, and A. D. Rae, J. Solid State Chem. **94**, 404 (1991).
[9] H. X. Yan, H. T. Zhang, R. Ubic, M. J. Reece, J. Liu, Z. J. Shen, and Z. Zhang, Adv. Mater. **17**, 1261 (2005).
[10] Z. G. Gai, J. F. Wang, M. L. Zhao, C. M. Wang, G. Z. Zang, B. Q. Ming, P. Qi, S. J. Zhang, and T. R. Shrout, Appl. Phys. Lett. **89**, 012907 (2006).
[11] X. P. Jiang, Q. Yang, S. L. Zhou, C. Chen, Y. Chen, N. Tu, and Z. D. Yu, J. Am. Ceram. Soc. **94**, 1109 (2011).
[12] Z. Y. Zhou, Y. C. Li, S. P. Hui, and X. L. Dong, Appl. Phys. Lett. **104**, 012904 (2014).
[13] C. B. Long, H. Q. Fan, and M. M. Li, Dalton Trans. **42**, 3561 (2013).
[14] Y. J. Wu, J. Chen, J. Yuan, J. Xing, Z. Tan, L. M. Jiang, Q. Chen, and J. G. Zhu, J. Appl. Phys. **120**, 194103 (2016).
[15] Z. Y. Zhou, X. L. Dong, H. Chen, and H. X. Yan, J. Am. Ceram. Soc. **89**, 1756 (2006).
[16] C. B. Long, H. Q. Fan, and P. R. Ren, Inorg. Chem. **52**, 5045 (2013).
[17] K. Homma and M. Wada, in *Proceedings of 1st Meeting on Ferroelectric Materials and Their Applications* (Ferro. Mater. Appl. Office, Kyoto, 1977), p. 165.
[18] S. Borg and G. Svensson, J. Solid State Chem. **157**, 160 (2001).
[19] S. Kamba, J. Pokorný, V. Porokhonskyy, J. Petzelt, M. P. Moret, A. Garg, Z. H. Barber, and R. Zallen, Appl. Phys. Lett. **81**, 1056 (2002).
[20] M. Maczka, L. Macalik, and J. Hanuza, J. Raman Spectrosc. **40**, 2099 (2009).
[21] H. C. Gupta, Archana, and V. Luthra, Vib. Spectrosc. **56**, 235 (2011).
[22] H. C. Gupta, Archana, and V. Luthra, J. Mol. Struct. **984**, 204 (2010).
[23] P. P. Jiang, X. L. Zhang, P. Chang, Z. G. Hu, W. Bai, Y. W. Li, and J. H. Chu, J. Appl. Phys. **115**, 144101 (2014).
[24] J. Z. Zhang, K. Jiang, Z. Y. Zhou, Z. G. Hu, G. S. Wang, X. L. Dong, and J. H. Chu, J. Am. Ceram. Soc. **99**, 3610 (2016).
[25] P. Lautenschlager, M. Garriga, L. Vina, and M. Cardona, Phys. Rev. B **36**, 4821 (1987).
[26] Q. L. Deng, J. Z. Zhang, T. Huang, L. P. Xu, K. Jiang, Y. W. Li, Z. G. Hu, and J. H. Chu, J. Mater. Chem. C **3**, 8225 (2015).
[27] Z. H. Duan, Z. G. Hu, K. Jiang, Y. W. Li, G. S. Wang, X. L. Dong, and J. H. Chu, Appl. Phys. Lett. **102**, 151908 (2013).
[28] K. Shi, L. Peng, M. J. Li, Z. Y. Zhou, K. Jiang, J. Z. Zhang, Z. G. Hu, X. L. Dong, and J. H. Chu, J. Alloys Compd. **653**, 168 (2015).
[29] M. P. Moret, R. Zallen, R. E. Newnham, P. C. Joshi, and S. B. Desu, Phys. Rev. B **57**, 5715 (1998).
[30] E. Buixaderas, D. Nuzhnyy, J. Petzelt, L. Jin, and D. Damjanovic, Phys. Rev. B **84**, 184302 (2011).
[31] F. Cordero, F. Trequattrini, F. Craciun, and C. Galassi, J. Phys.: Condens. Matter **23**, 415901 (2011).
[32] M. A. Subramanian, D. Li, N. Duan, B. A. Reisner, and A. W. Sleight, J. Solid State Chem. **151**, 323 (2000).
[33] S. P. Pavunny, A. Kumar, and R. S. Katiyar, J. Appl. Phys. **107**, 013522 (2010).

[34] E. Buixaderas, I. Gregora, J. Hlinka, J. Dec, and T. Łukasiewicz, Phase Transitions **86**, 217 (2013).
[35] K. R. Whittle, N. C. Hyatt, and I. M. Reaney, Chem. Mater. **20**, 6427 (2008).
[36] R. M. A. Azzam and N. M. Bashara, *Ellipsometry and Polarized Light* (North-Holland, Amsterdam, 1977).
[37] A. B. Djurišić, Y. Chan, and E. H. Li, Mater. Sci. Eng. R **38**, 237 (2002).
[38] D. A. G. Brüggeman, Ann. Phys. (Leipzig) **416**, 636 (1935).
[39] G. E. Jellison and F. A. Modine, Appl. Phys. Lett. **69**, 371 (1996); **69**, 2137 (1996).
[40] D. V. Likhachev, N. Malkova, and L. Poslavsky, Thin Solid Films **589**, 844 (2015).
[41] A. Peláiz-Barranco and Y. González-Abreu, J. Adv. Dielectr. **03**, 1330003 (2013).
[42] J. Z. Zhang, W. Y. Tong, J. J. Zhu, J. Y. Xu, Z. H. Duan, L. P. Xu, Z. G. Hu, C. G. Duan, X. J. Meng, Z. Q. Zhu, and J. H. Chu, Phys. Rev. B **91**, 085201 (2015).
[43] H. B. Shu, L. Z. Sun, X. L. Zhong, J. B. Wang, and Y. C. Zhou, J. Phys. Chem. Solids **70**, 707 (2009).
[44] J. P. Perdew, K. Burke, and M. Ernzerhof, Phys. Rev. Lett. **77**, 3865 (1996).
[45] J. M. Perez-Mato, M. Aroyo, A. García, P. Blaha, K. Schwarz, J. Schweifer, and K. Parlinski, Phys. Rev. B **70**, 214111 (2004).
[46] R. E. Cohen, Nature (London) **358**, 136 (1992).
[47] Y. E. Kitaev, M. I. Aroyo, and J. M. Perez-Mato, Phys. Rev. B **75**, 064110 (2007).